

Tribological Properties of Hard Metal Coatings Sprayed by High-Velocity Air Fuel Process

C. Lyphout, K. Sato, S. Houdkova, E. Smazalova, L. Lusvarghi, G. Bolelli, and P. Sassatelli

(Submitted April 2, 2015; in revised form July 16, 2015)

Lowering the thermal energy and increasing the kinetic energy of hard metal particles sprayed by the newly developed HVAF systems can significantly reduce their decarburization, and increases the sliding wear and corrosion resistance of the resulting coatings, making the HVAF technique attractive, both economically and environmentally, over its HVOF predecessors. Two agglomerated and sintered feed-stock powder chemistries, WC-Co (88/12) and WC-CoCr (86/10/4), respectively, with increasing primary carbides grain size from 0.2 to 4.0 microns, have been deposited by the latest HVAF-M3 process onto carbon steel substrates. Their dry sliding wear behaviors and friction coefficients were evaluated at room temperature via Ball-on-disk (ASTM G99-90) wear tests against Al_2O_3 counterparts, and via Pin-on-disk (ASTM G77-05) wear tests against modified martensitic steel counterparts in both dry and lubricated conditions. Sliding wear mechanisms, with the formation of wavy surface morphology and brittle cracking, are discussed regarding the distribution and size of primary carbides. Corrosion behaviors were evaluated via standard Neutral Salt Spray, Acetic Acid Salt Spray, accelerated corrosion test, and electrochemical polarization test at room temperature. The optimization of the tribological properties of the coatings is discussed, focusing on the suitable selection of primary carbide size for different working load applications.

Keywords carbides grain size, corrosion, hard metal, HVAF, HVOF, sliding wear, tribology

1. Introduction

In the field of protective coatings against wear and corrosion, recent restrictions in the use of the carcinogenic hexavalent form of chromium have driven the need of replacing Electrolytic Hard Chrome plating (EHC) by other materials/processes with equivalent tribological properties (Ref 1). Alternatives to EHC have emerged in the past decades in the field of thermal spray technology, which also allowed an improvement of the surface properties of critical components (Ref 2, 3), such as hydraulic pistons, ball valves, turbine valves, rolls and plungers, found in oil production systems, hydroelectric power plants, paper and mining industries, and desalination

This article is an invited paper selected from presentations at the 2015 International Thermal Spray Conference, held May 11-14, 2015, in Long Beach, California, USA, and has been expanded from the original presentation.

C. Lyphout, University West, Trollhättan, Sweden; K. Sato, Fujimi Incorporated, Kakamigahara, Japan; S. Houdkova and E. Smazalova, University of West Bohemia, Plzeň, Czech Republic; and L. Lusvarghi, G. Bolelli, and P. Sassatelli, University of Modena and Reggio Emilia, Modena, Italy. Contact e-mails: christophe.lyphout@hv.se, atouk@fujimiinc.co.jp, houdkova@ntc.zcu.cz, and luca.lusvarghi@unimore.it.

plants. In this field of application, cermet materials have been widely applied by several generations of HVOF systems (Ref 4), and more recently by HVAF ones (Ref 5-7). The interest in ceramic-metal composites is to combine optimal material properties of both a ceramic, such as high temperature stability and hardness, and those of a tough metal, such as the ability to undergo plastic deformation. Hard WC or Cr_3C_2 particles, which perform as the major wear-resistant constituent, are embedded in a Co-/CoCr-/NiCr-based matrix, providing toughness, support, and playing a critical role against oxidation and corrosion. Generally, the choice of carbides chemistry is dictated by the application temperature: WC is generally preferred over Cr_3C_2 if temperatures do not exceed 200 °C, which provides low wear and low friction coefficient, whereas Cr_3C_2 -based systems might exhibit stable and lower friction at elevated temperature (Ref 5). The wear resistance of cermet coatings may however decrease at higher load conditions. Therefore, the challenges are to understand to how intra-lamellar features (e.g., carbide size and carbide-matrix interface cohesion) and inter-lamellar cohesion influence the tribological performances of the coating under different working conditions, varying in terms of e.g., applied load, velocity, temperature, lubrication, abrasive size/media, and environments (Ref 8). Among several standard tribological test methods, ASTM G99 (Ref 9) and ASTM G77 (Ref 10) cover laboratory procedures to rank the sliding wear resistance of protective coatings. Several types of lubricants, temperature, and load conditions can be tuned for each method in order to represent the targeted working conditions. Three main

features characterize the microstructure of cemented carbides: (1) the Carbide Grain Size (CGS), (2) the Carbides Contiguity (CC), and (3) the Binder Mean Free Path (MFP). However, the difficulty in evaluating those microstructural features has led to contradictory trends (Ref 11), regarding the influence of matrix content and primary carbides size on the tribological properties of the coating. Common errors include (1) missing a significant but relatively small fraction of large carbides that carry most of the volume and mass of their own distribution, and (2) missing a relatively large number of significant but small carbides that carry most of the number-weighted information. In the present study, efforts have been made (1) to quantify weighted distributions of microstructural features, such as CGS, CC, and MFP, and (2) to investigate the relationships between those microstructural features and the resulting sliding wear resistance of WC-based HVOF-sprayed coatings, carrying out standardized tests such as ASTM G77-05 and ASTM G99-90. The corrosion resistance and corrosion mechanisms of these coatings are also of particular technical and scientific interest; hence, they were investigated via cyclic cabinet tests and electrochemical polarization tests.

2. Experimental Procedure

2.1 Spray Process and Feedstock Materials

Two agglomerated and sintered tungsten carbide powders with either Co matrix or CoCr matrix, and increasing Carbide Grain Sizes (CGS) from 0.2 to 4.0 μm , were manufactured by Fujimi Inc. (Table 1). All powders had identically fine particle size distribution ($-30 + 5 \mu\text{m}$), and they were all deposited up to twelve passes with the HVOF-M3 system (UniqueCoat, US), using the spray parameters developed in a previous work (Ref 12). The HVOF-M3 process is a “hardware-based” high-velocity thermal spray process, i.e., various combinations of combustion chamber, nozzle, and injector are available, each one being specific to a sweet spot which can barely operate outside a tiny process window without becoming unstable. Each hardware combination can be optimized for a specific material chemistry. This confers a processing robustness to each configuration for a selected material, which has been investigated previously by the authors (Ref 13). In the present study, a standard configuration,

i.e., operating the large combustion chamber, long nozzle, and short injector, has been selected to apply the different WC-based powder feedstock materials. Prior to spraying, the low carbon steel (Domex355) substrates, positioned onto a carousel, were grit blasted using the HVOF-M3 system itself. Both feedstock chemistries were also HVOF sprayed utilizing a JP5000 gun, considering a slightly coarser powder cut ($-45 + 15 \mu\text{m}$) with medium CGS of 2.0 μm . An EHC sample was further utilized as a reference for the targeted application (Ref 12).

2.2 Characterization Methods

2.2.1 Microstructure. Coating cross sections were analyzed utilizing a Scanning Electron Microscope (Jeol JSM-7800F) with acceleration voltage of 10.0 kV. An image analysis procedure utilizing Aphelion[®] software coupled with Matlab[®] was developed in a previous work (Ref 12) and improved in the present study for SEM micrographs with higher magnifications ($\times 20,000$) with a dimension of 1200×940 pixels. For each coating, 20 evenly distributed fields were analyzed on one cross section for each sample to evaluate (1) the volume fraction of coating porosity and carbide/binder phases, and (2) weighted distributions of primary carbides grain size (CGS), Carbides Contiguity (CC), and binder Mean Free Path (MFP).

2.2.2 Sliding Wear Resistance. A ball-on-disk tribological test (Pin-on-Disk Tribometer, Anton-Paar TriTec, Peseux, Switzerland) was conducted according to ASTM G99-90 to investigate the dry sliding wear resistance of the coating. The tests were performed both under room temperature conditions (25 °C and $\approx 60\%$ relative humidity) and at 400 °C. In the latter case, the samples were heated through the base plate of the pin-on-disk tribometer and their temperature was measured with a thermocouple in contact with their rear face. For each test temperature, two samples for each set, with dimension 22 mm \times 22 mm, were polished to $R_a = 0.01 \mu\text{m}$ and tested against a 6-mm diameter Al_2O_3 ball as counterpart. Tests were conducted at 10 N normal load, 0.10 m/s relative sliding speed, 5000 m sliding distance. The sample wear volume was measured by optical confocal profilometry (Conscan profilometer, Anton-Paar TriTec). Data are then converted to wear rate (defined as the wear volume per unit sliding distance) and coefficient of wear (COW), defined as the wear volume per unit sliding distance and unit normal load. Wear scars were observed by SEM;

Table 1 Powder feedstock materials and processes

Ref.	Spraying process	Chemical composition	Particles size (μm)	Carbides size (μm)
P1K1	HVOF-M3	WC-Co 88/12	$-30 + 5$	0.2
P1K2	HVOF-M3	WC-Co 88/12	$-30 + 5$	2.0
P1K3	HVOF-M3	WC-Co 88/12	$-30 + 5$	4.0
P1K4	HVOF-M3	WC-CoCr 86/10/4	$-30 + 5$	0.2
P1K5	HVOF-M3	WC-CoCr 86/10/4	$-30 + 5$	2.0
P1K6	HVOF-M3	WC-CoCr 86/10/4	$-30 + 5$	4.0
P2K2	HVOF-JP	WC-Co 88/12	$-45 + 15$	2.0
P2K5	HVOF-JP	WC-CoCr 86/10/4	$-45 + 15$	2.0
EHC	Electrolytic	

additional investigations included micro-Raman spectrometry (Lab-Ram micro-spectrometer, Horiba Jobin-Yvon, Villeneuve D'Ascq, France; laser wavelength: 632.81 nm) to assess the structure of the wear debris collected on the samples after the test, and transmission electron microscope (TEM: JEM 2010, Jeol, Tokyo, Japan) observation of the same.

In order to support the interpretation of wear mechanisms, scratch tests (Micro-Combi Tester, Anton-Paar TriTec) were also performed on some of the polished samples, using a Rockwell C-type conical diamond indenter with 200- μm radius spherical tip. The load was linearly increased from 0.01 to 30 N over a scratch length of 6 mm, with an advancing speed of 1 mm/min. For each tested sample, three scratch tracks were performed and inspected by optical microscopy.

The block-on-ring tribological test (CETR-UMT3 Tribometer, BRUKER) was as well conducted according to ASTM G77-05. Samples were prior polished to $R_a=0.1$ μm , and tested at room temperature using a modified martensitic bearing steel (DIN 100CrMnSi6-4) ring as counterpart. Tests were conducted at 1.37 m/s relative sliding speed, for a total sliding distance of 7000 m with discontinuous sequences, and at 40-60% relative humidity. Loads of 75 N and 250 N were selected under dry conditions, and loads of 500 and 750 N under lubricated conditions utilizing a standard mineral oil-based lubricant (SAE 15W-40, VW 501.01, VW 505.00). Wear scar dimensions were measured using a profilometer (KLA-Tencor P-6) and investigated by SEM.

2.2.3 Cyclic Corrosion Resistance. The samples were polished to $R_a=0.1$ μm , their edges were protected by a specially designed strip of silicone sealant, and the as-polished surface was exposed to cyclic corrosive environment. The salt spray test was carried out according to ISO 16701, utilizing ASCOTT CC450XP equipment to expose samples to a maximal period of 80 and 192 h, for AASS (Acetic Acid Salt Spray) and NSS (Neutral Salt Spray) environments, respectively. Accelerated corrosion (Corrodokote) test was also carried out according to ASTM B380-97, subjecting the samples (polished to $R_a=0.01$ μm and protected by a silicone sealant along their edges) to five cycles of 20 h each. At the beginning of each cycle, a slurry, which consists of 30 g of kaolin and 50 mL of a solution containing copper nitrate, ferric chloride, and ammonium chloride, is applied onto the samples. These are kept in a test chamber at 38 °C and 85% relative humidity for the entire cycle duration. All damage degrees of the exposed surfaces were evaluated by visual inspection after removing the corrosive slurry with running water. Complementary SEM and Energy-Dispersive x-ray Spectroscopy (EDS) microanalysis of the cross sections of corroded systems were also performed in order (1) to identify the chemical composition of observed phases and corroded products, and (2) to investigate the possible corrosion mechanisms.

2.2.4 Polarization Test. The corrosion behavior of the coated samples was as well studied by electrochemical

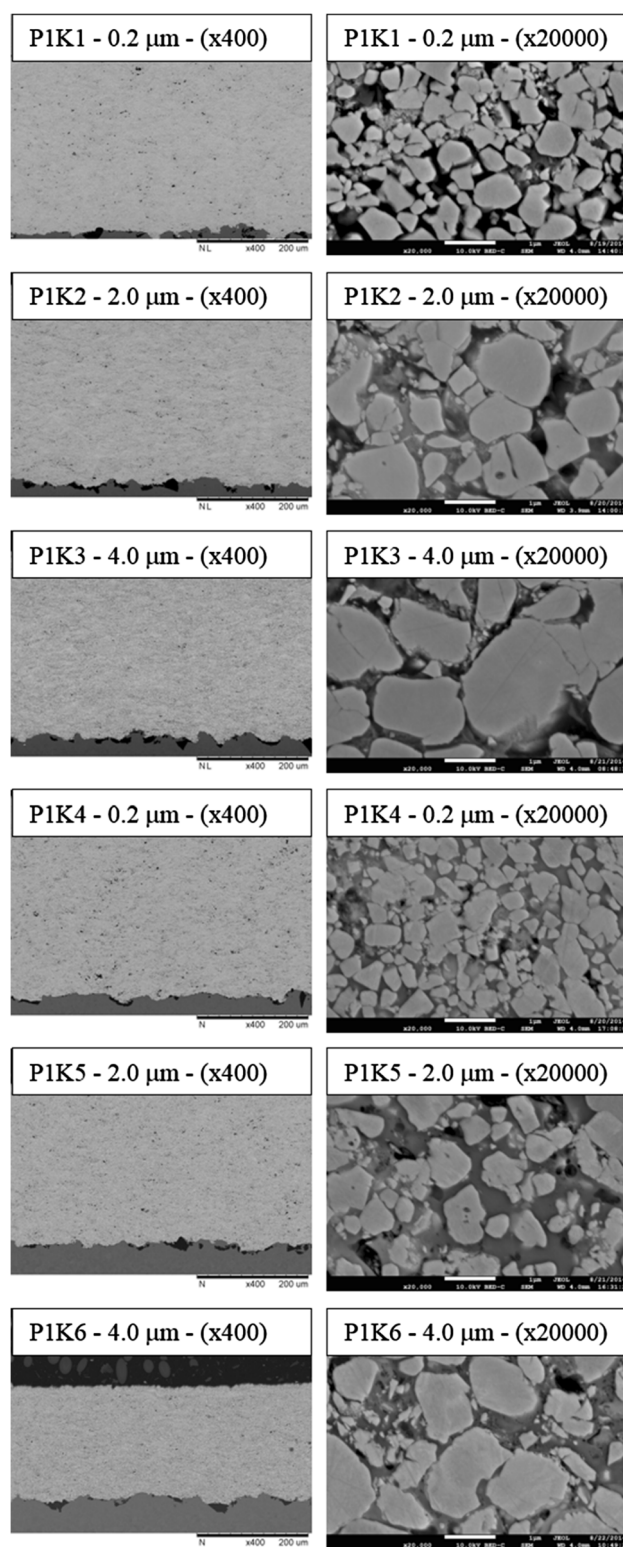


Fig. 1 SEM micrographs of respective HVAF-sprayed coatings, from fine and medium to coarse CGS; and respective BSEM micrographs at high magnification ($\times 20,000$) utilized for the Image Analysis method to evaluate respective microstructure features distributions

Table 2 Volume fraction of microstructure features and weighted distribution characteristics for the carbides grain size (CGS), the carbides contiguity (CC), and the mean free path (MFP), respectively

	P1K1	P1K2	P1K3	P1K4	P1K5	P1K6
Porosity (%)	0.48 ± 0.32	0.39 ± 0.25	0.35 ± 0.18	1.07 ± 0.46	2.10 ± 0.78	1.14 ± 0.35
Carbide (%)	75.5 ± 5.84	74.5 ± 4.60	70.0 ± 4.52	68.6 ± 3.47	61.3 ± 2.03	57.1 ± 3.54
Binder (%)	24.0 ± 5.91	25.1 ± 4.48	29.6 ± 4.47	30.4 ± 3.25	36.6 ± 2.08	41.8 ± 3.53
CGS (μm)	0.59 ± 0.07	0.88 ± 0.12	1.30 ± 0.56	0.50 ± 0.04	0.75 ± 0.12	1.11 ± 0.54
D_{CGS} (μm ⁻²)	5.5	3.0	2.6	6.8	4.0	3.3
FWHM (μm)	0.517	0.851	1.675	0.429	0.735	1.232
CC (μm)	0.46 ± 0.04	0.72 ± 0.11	0.83 ± 0.22	0.41 ± 0.03	0.59 ± 0.09	0.76 ± 0.27
D_{CC} (μm ⁻²)	5.8	3.5	1.8	7.7	3.3	2.2
FWHM (μm)	0.461	0.849	1.087	0.399	0.658	0.831
MFP (μm)	0.29 ± 0.08	0.34 ± 0.09	0.55 ± 0.23	0.26 ± 0.07	0.40 ± 0.15	0.56 ± 0.24
D_{MFP} (μm ⁻²)	3.8	1.8	5.0	3.9	4.5	7.8
FWHM (μm)	0.615	0.719	1.239	0.540	0.922	1.298

polarization test at room temperature. The tests were performed using a 3-electrode cell containing approximately 300 mL of a 0.1 M HCl solution. The coated sample, having an exposed surface of 1 cm², is connected to the working electrode; a Pt grid is used as counter electrode and a Ag/AgCl/KCl_(3M) electrode acts as reference. The polarization test was started after 1 h of free corrosion, in order to allow stabilization of the system. Starting from the open circuit potential (OCP), the coated samples were cathodically polarized up to -400 mV versus OCP and then anodically polarized up to +1400 mV versus OCP at a rate of 0.5 mV/s. The Tafel method was applied to fit detectable linear portions of both cathodic and anodic polarization curves. The coordinates of the intersection point identify the corrosion potential (E_{Corr}) and the corrosion current density (I_{Corr}) of the system.

3. Results and Discussions

3.1 Microstructure

In a general observation, coatings density was improved when increasing the carbides grain size (Fig. 1), following the trend from K1 to K3 for WC-Co, and from K4 to K6 for WC-CoCr feedstock materials. This was attributed to the relative increase of the volume fraction of binder material (Table 2). The conventionally high deposition efficiency (75-80%) dropped approximately to 65-70% with coarsening of the primary carbides size, due to the erosion/abrasion of the pre-deposited layer by larger impinging particles momentum. W₂C and W phases, derived from thermal decomposition of the powder during spraying, were found predominantly in the HVOF-sprayed coatings compared to the HVAF deposits, as previously demonstrated by the authors through XRD analysis on both feedstock and resulting coated materials (Ref 12). Those results highlight the relatively colder conditions observed in HVAF compared to HVOF process. The microstructural features of the corresponding coatings were evaluated by image analysis as described previously. Carbides were identified and defined by either their geometry (area, contour, and center of mass position) or categorized regarding their equivalent diameter

size. In a first attempt, CGS, CC, and MFP number-weighted distributions were computed and evaluated. However, due to the broad population of CGS values, a relatively large number (>80%) of small carbides (<0.05 μm) carry most of the number-weighted information, leading to the inadequate representation of a relatively small number (<5%) of large carbides (>3.00 μm), which, by virtue of their size, carry most of the area-weighted information. Therefore, an area-weighted function has been applied to CGS distribution by multiplying the number-weighted distribution by the square of carbides equivalent diameter 14. Similarly, a discrete length-weighted function has been applied to the CC distribution by multiplying the number-weighted distribution by the respective distances relatively to the perimeters of intercepting carbides (Ref 14). Last but not least, a discrete length-weighted function has been applied to the MFP distribution by multiplying the number-weighted distribution by the respective MFP length relatively to the volume fraction of the binder phase. Respective carbides density (D_{CGS}), carbide contacts density (D_{CC}), and carbide-to-carbide distance density (D_{MFP}) were calculated, accordingly to the cross-section surface area sampled through the 20 observed fields for each coating (Table 2). For each weighted distribution, its mean, standard deviation, and full width at half maximum (FWHM) values were evaluated in order to quantify the differences observed in distribution shapes. The coarser the CGS, the lower the D_{CGS} . The bigger the CGS, the higher CC, to the detriment of D_{CC} . The MFP and its density are shown to increase with the carbide size, which is in accordance with the increase of the binder volume fraction in the respective series (Table 2). For all microstructure features, broadening of the weighted distributions with the coarsening of the CGS is quantified by the increase of the respective FWHM values. Such broadening is responsible for increasing the values of the standard deviations of the respective weighted-mean values of CGS, CC, and MFP.

3.2 Sliding Wear Test: ASTM G77-05

Under dry sliding wear at low load (75 N) conditions, the lowest coefficients of friction (COF) were found for coatings with medium CGS (2.0 μm), independently of the

Table 3 Sliding wear ASTM G77-05 results—tests carried out at room temperature, under different loading/lubricating conditions

Ref.	Process	Material	CGS (μm)	Load: 75 N/No lubrication			Load: 250 N/No lubrication			Load: 500 N/Lubrication			Load: 750 N/Lubrication		
				COF	Wear rate (10^{-5} mm ³ /m)	COW (10^{-7} mm ³ /Nm)	COF	Wear rate (10^{-5} mm ³ /m)	COW (10^{-7} mm ³ /Nm)	COF	Wear rate (10^{-7} mm ³ /m)	COW (10^{-9} mm ³ /Nm)	COF	Wear rate (10^{-7} mm ³ /m)	COW (10^{-9} mm ³ /Nm)
EHC	0.76 ± 0.07	32.2 ± 5.91	42.9 ± 7.87	0.57 ± 0.05	511 ± 80.5	204 ± 32.2	0.10 ± 0.01	9.71 ± 3.40	1.94 ± 0.68	0.10 ± 0.01	12.9 ± 2.48	1.72 ± 0.33
PIK1	HVAF-M3	WC-Co	0.2	0.76 ± 0.14	1.75 ± 0.34	2.33 ± 0.46	0.55 ± 0.05	0.61 ± 0.16	0.24 ± 0.06	0.13 ± 0.01	7.54 ± 1.71	1.51 ± 0.34	0.12 ± 0.01	9.29 ± 2.94	1.24 ± 0.39
PIK2	HVAF-M3	WC-Co	2.0	0.71 ± 0.24	0.63 ± 0.12	0.85 ± 0.16	0.55 ± 0.05	0.85 ± 0.60	0.34 ± 0.24	0.13 ± 0.01	9.17 ± 3.43	1.83 ± 0.68	0.12 ± 0.01	6.04 ± 0.66	0.80 ± 0.09
PIK3	HVAF-M3	WC-Co	4.0	0.85 ± 0.13	4.11 ± 0.25	5.48 ± 0.34	0.56 ± 0.06	0.79 ± 0.08	0.32 ± 0.03	0.12 ± 0.01	11.9 ± 7.27	2.37 ± 1.45	0.11 ± 0.01	7.81 ± 1.89	1.04 ± 0.25
P2K2	HVOF-JP	WC-Co	2.0	0.79 ± 0.15	2.42 ± 0.60	3.22 ± 0.79	0.53 ± 0.05	4.04 ± 0.23	1.62 ± 0.91	0.12 ± 0.01	10.5 ± 5.09	2.10 ± 1.24	0.10 ± 0.01	5.56 ± 0.74	0.74 ± 0.10
PIK4	HVAF-M3	WC-CoCr	0.2	0.77 ± 0.10	1.87 ± 1.02	2.49 ± 1.37	0.56 ± 0.05	1.68 ± 0.70	0.67 ± 0.28	0.12 ± 0.01	8.57 ± 5.09	1.71 ± 1.02	0.10 ± 0.01	7.53 ± 1.69	1.00 ± 0.23
PIK5	HVAF-M3	WC-CoCr	2.0	0.70 ± 0.08	0.77 ± 0.20	1.02 ± 0.27	0.57 ± 0.05	0.98 ± 0.86	0.39 ± 0.34	0.11 ± 0.01	8.54 ± 2.10	1.71 ± 0.42	0.10 ± 0.01	4.62 ± 2.03	0.61 ± 0.27
PIK6	HVAF-M3	WC-CoCr	4.0	0.87 ± 0.15	4.01 ± 0.38	5.34 ± 0.50	0.53 ± 0.05	0.76 ± 0.26	0.30 ± 0.10	0.11 ± 0.01	9.84 ± 3.17	1.97 ± 0.63	0.10 ± 0.01	4.74 ± 0.64	0.63 ± 0.08
P2K5	HVOF-JP	WC-CoCr	2.0	0.78 ± 0.13	0.51 ± 0.06	0.68 ± 0.09	0.56 ± 0.05	0.61 ± 0.54	0.25 ± 0.22	0.13 ± 0.01	10.7 ± 6.97	2.14 ± 1.39	0.10 ± 0.01	6.32 ± 2.53	0.84 ± 0.34

spraying technique (HVAF or HVOF) (Table 3). To the contrary, decreasing the CGS to 0.2 μm or increasing it to 4.0 μm , both friction and wear slightly increase, likely highlighting a change in the wear mechanism, respectively, from inter-lamellar levels for finer CGS, to intra-lamellar levels for coarser CGS. The ratio between the CGS and the matrix grain size plays here a critical role in the coating behavior under mechanical loading, leading to a more suitable tribological balance in the present study with the 2.0 μm CGS. Increasing the load to 250 N under dry sliding conditions, the COF dropped to a value of 0.55 for all coated systems, independently of the CGS, material, or spray process. For each composition, the wear rates do not differ much from one another as a function of CGS (taking the associated standard deviation into account); however, it seems that HVAF WC-Co coatings attain minimum wear loss with the finest CGS, while coarse CGS is more favorable for HVAF WC-CoCr coatings. Under lubricated conditions, the same trend is observed as under dry conditions, at much lower levels for both wear rate and COW. The COF dropped to an average value of ≈ 0.11 , with a slight decreasing tendency with increasing CGS. As previously observed under dry conditions, increasing the load under lubricated conditions generally reduces the wear rate and COW, independently of the COF. However, the trend with CGS variations is reversed at higher load: wear rate and COW increases with CGS at low load, whereas, under higher load conditions, an intermediate CGS value of 2.0 μm seems preferable. It should however be remarked that, for a given load, all differences between samples belonging to the same group are very small. On the other hand, WC-CoCr samples seem to be superior to WC-Co ones under lubricated conditions at high load. Based on Fig. 2, wear under dry conditions is dominated by abrasive grooving with minor brittle fracture, whereas carbide pull-out is observed under lubricated conditions, indicating wear by surface fatigue. This can be better restrained in WC-10Co4Cr due to the higher matrix content resulting in higher toughness, due to better wetting between carbides and the matrix. Under both dry loading conditions, the sprayed coatings outperform the EHC reference by a few orders of magnitude, for similar values of coefficients of friction. Under lubricated conditions, the sprayed coatings exhibit similar wear rate and COW than the EHC reference at low load (500 N), whereas both HVOF and HVAF coatings outperformed the EHC sample at higher load (750 N).

3.3 Sliding Wear Test: ASTM G99-90 (Room Temperature)

At room temperature, all coated systems corresponded to a mild wear regime (Fig. 3), and exhibited a coefficient of wear (COW) three orders of magnitude lower than the one obtained for the EHC reference. At lower magnification (Fig. 4), all samples seem to exhibit mild abrasive grooves. At higher magnification, it is however seen that this grooving process is controlled by two distinct wear mechanisms, depending on the CGS. Individual coarse carbide particles bear the entire contact stress between the

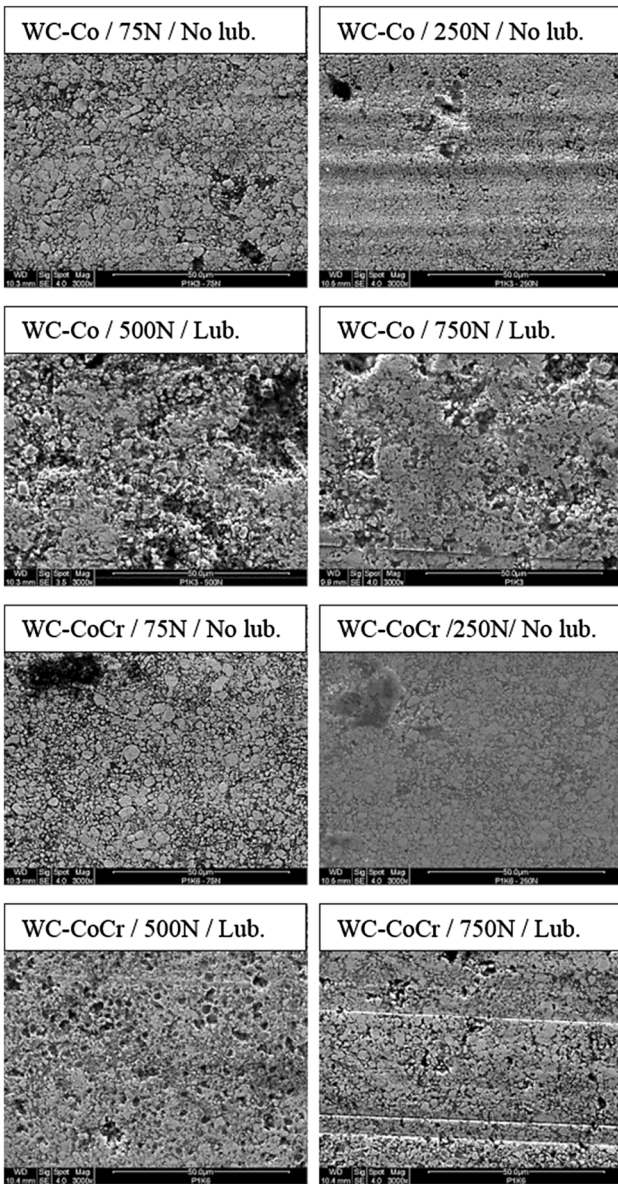


Fig. 2 BSEM micrographs of HVOF coatings with coarse primary carbides (4.0 μm) after sliding wear G77-05 tests

coating and the counter body asperities, leading to micro-scale plastic deformation and cracking inside the carbides themselves, a phenomenon more predominant for WC-Co (P1K3)- than WC-CoCr (P1K6)-coated materials (Fig. 5). The possible occurrence not only of brittle cracking, but also of localized plastic slip inside WC grains under sliding contact has been confirmed in (Ref 15) through scratch testing experiments on cermets. For fine-grained structure (P1K1/P1K4), the load is distributed on several grains and on the surrounding matrix. The latter flows plastically, under the action of the out-of-plane shear stress induced by the friction force, dragging WC grains onto the surface and pulling them out. This mechanism has also been predicted by microstructure-based finite element simulations in (Ref 16), and it has accordingly been observed by

the authors in other HVOF-sprayed WC10Co4Cr coatings with similarly fine carbide grain size (Ref 6). Those HVOF-sprayed coatings, however, were also affected by brittle fracture and near-surface delamination to some extent.

In any case, both mechanisms lead to the formation of a wavy surface morphology (Fig. 5) and eventually result in the bearing surface consisting almost uniquely of WC. All samples therefore produce nearly identical friction coefficient values of ≈ 0.45 (Fig. 3b). Due to its high hardness and low chemical reactivity, the counterpart surface remains clean and free of transfer material (Fig. 6).

The mild wear regime of all cermet coatings is witnessed not only by the low COW values ($\leq 1 \times 10^{-7} \text{ mm}^3/(\text{Nm})$, Fig. 3), as mentioned previously, but also by the very fine size of the debris particles (Fig. 7a). Fine debris is indeed typical of a mild wear condition (Ref 17). It consists of micrometric or sub-micrometric particles (Fig. 7a), some of which actually consist of nanoparticle aggregates (Fig. 7b). Some of these nanoparticles are crystalline (Fig. 7c), which probably indicates the presence of small fragments of pulled-out WC particles, but a large amorphous component exists, as testified by the halo found in typical selected-area electron diffraction (SAED) patterns (Fig. 7d). Accordingly, the debris also contains non-crystalline, hydrated tungsten oxides: their presence, testified by the broad peak at about 960 cm^{-1} (Ref 18, 19) in the Raman spectra of the debris (Fig. 8), is a clear consequence of tribo-oxidation of such extremely fine (hence, highly reactive) particles exposed to the air environment.

The previous mechanism highlights how the carbide-matrix interfaces influence the coating tribological performances. For Co matrix feedstock, no significant difference in coating wear properties could be noticed between HVOF and HVOF processes, and this independently of the primary carbides size (Fig. 3). However, for CoCr matrix feedstock, HVOF-sprayed coatings exhibited higher sliding wear resistance than HVOFs. Moreover, for the WC-CoCr composition, the COW decreases with increasing CGS, which is similar to the tendency observed in dry ASTM G77-05 testing of WC-CoCr coatings at high load. The cohesion between carbides and matrix material for HVOF coatings appears to be worse than for HVOF deposits, leading to pull-outs and excessive wear (Fig. 4, 5). This result is quite consistent with the previously recalled findings in (Ref 6) and with other literature studies on the wear behavior of HVOF-sprayed WC-based cermets (Ref 7, 20, 21). The HVOF processing has indeed been shown to lead to a higher degree of decarburization for this specific chemical composition, altering the interaction between matrix and carbides (Ref 7). This reportedly leads to greater incidence of brittle cracking and localized pull-outs from the coating surface during sliding contacts (Ref 7, 20, 21), increasing the wear loss in the studied sliding wear regime. On the other hand, attempting to reduce decarburization and carbide dissolution by lowering the HVOF flame temperature is also ineffective to improve the sliding wear resistance, as discussed in (Ref 21). In the extreme case when HVOF process conditions are particularly “cold,” as in the study by Yang

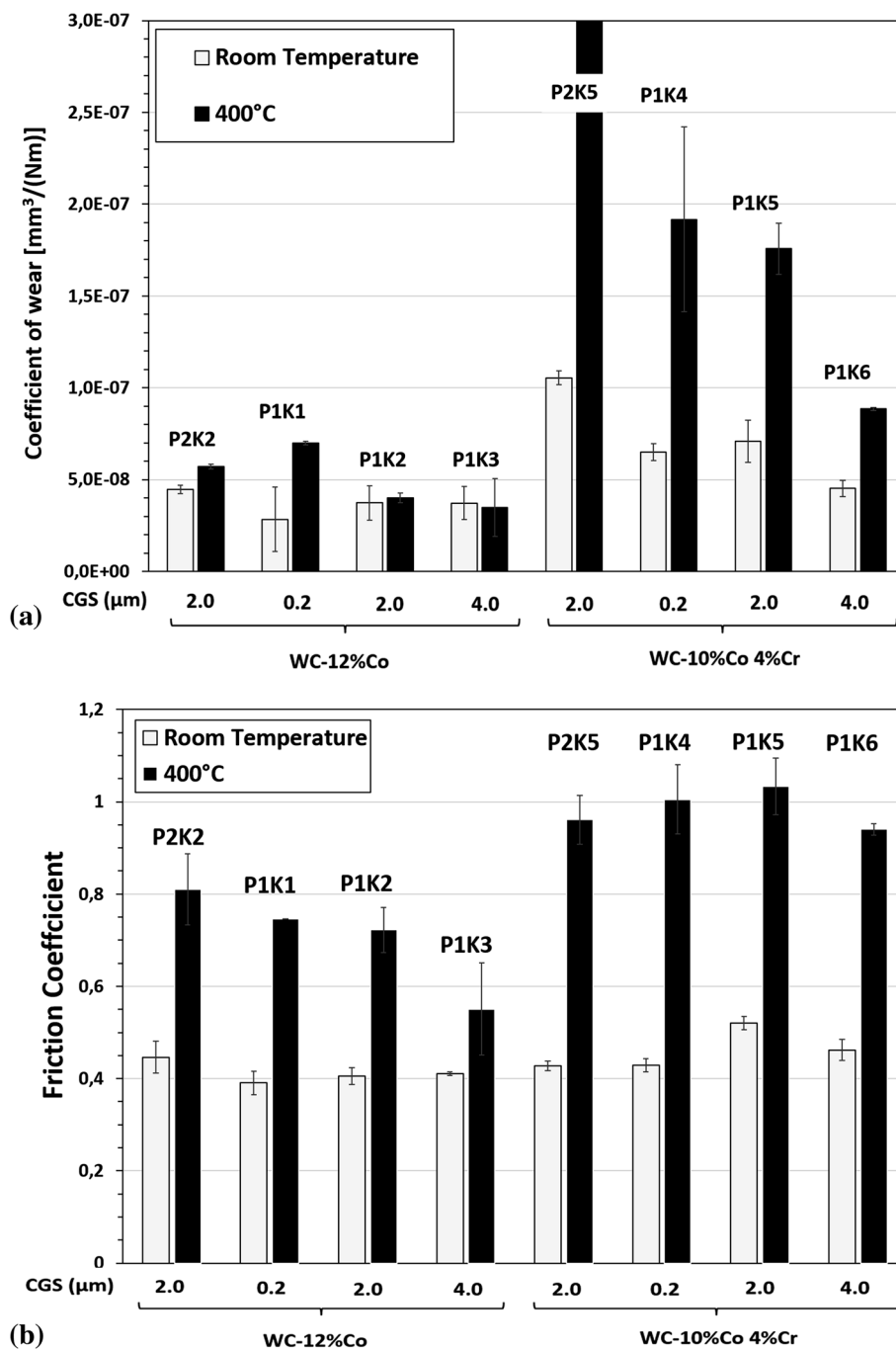


Fig. 3 Coefficient of wear (a) and average friction coefficient (b) recorded after ball-on-disk G99-90 testing of all samples against the alumina counterbody at room temperature and at 400 °C

et al. (Ref 22, 23), coatings have remarkably high porosity (>6 vol.%), which is usually undesirable and typically avoided for practical applications. In those coatings, the ductile β -Co phase is still identifiable through XRD patterns, which is a quite uncommon occurrence (Ref 24), and wear during sliding against an Al_2O_3 counterbody is due to the extrusion of such soft matrix, followed by the pull-out of entire, unsupported WC grains. A tribofilm is then formed by plastic smearing of the resulting wear

debris (Ref 22, 23). For such coatings, higher wear loss occurs with coarse WC grains under all loading conditions, which is in contrast with the present results.

The present results therefore indicate that WC-based coatings obtained by the HVAF process, on account of the higher particle velocities and lower temperatures (compared to standard HVOF processes) (Ref 25), suffer minimal brittle fracture wear but, at the same time, possess stronger carbide-matrix cohesion: plastic deformation

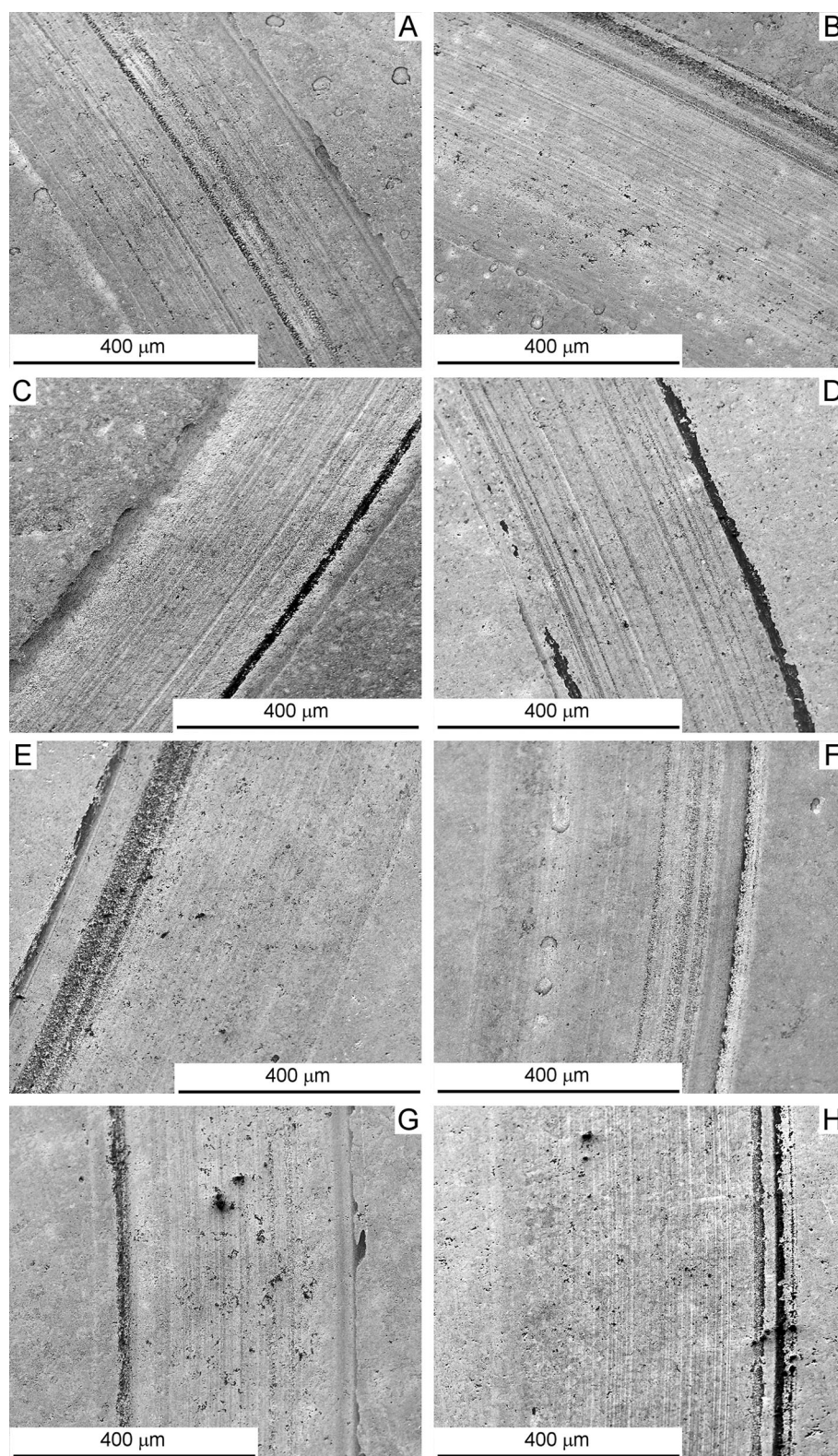


Fig. 4 SEM micrographs (secondary electrons) of the worn surface of samples P1K1 (a), P1K2 (b), P1K3 (c), P1K4 (d), P1K5 (e), P1K6 (f), P2K2 (g), and P2K5 (h) after ball-on-disk G99-90 testing at room temperature

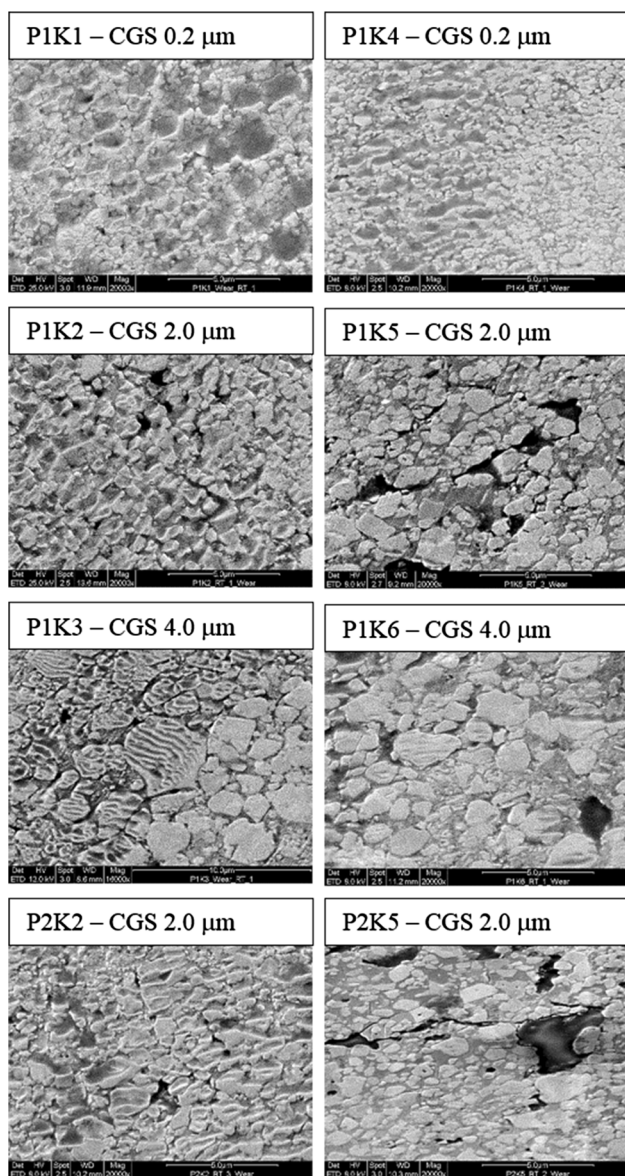


Fig. 5 High-resolution SEM micrographs to observe wear mechanisms of worn surfaces after ball-on-disk G99-90 testing at room temperature

of the cermet system therefore occurs without those extreme Co extrusion and pull-out conditions as encountered in (Ref 22). In particular, the ratio of the primary carbide grain size to the binder material size appears to be a key parameter to explain the sliding wear behavior of coated systems. Such correlations are nowadays being studied by the main author (Ref 14) through a Design of Experiment based on powder feedstock features. Such screening approach has the potential to draw statistical correlations among Carbides Grain Size (CGS), Binder Grain Size (BGS), and the initial Powder Strength (PS) to design HVAF-sprayed coatings with advanced tribological properties. Preliminary results (Ref 14) show that coarsening the CGS can lead to detrimental sliding wear

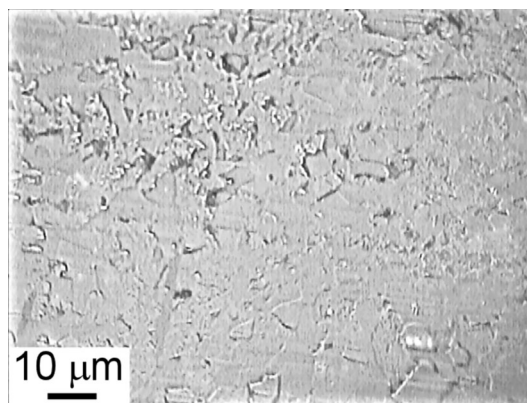


Fig. 6 Optical micrograph of the worn surface of the Al_2O_3 counterbody after ball-on-disk sliding wear testing against sample P1K6 at room temperature

behavior if combined with both coarse BGS and higher PS than the one considered in this study.

3.4 Sliding Wear Test: ASTM G99-90 (400 °C)

At 400 °C, the advantage given by the coarse CGS becomes even more obvious (Fig. 3a). Additional features appear as follows:

- (1) The COW of the WC-10Co4Cr coatings increases remarkably, whereas that of the WC-12Co coatings is nearly unaltered (apart from the sample with the finest CGS).
- (2) Coarse CGS becomes advantageous even in the case of WC-Co, a behavior which differs from that encountered at room temperature (both under ball-on-disk conditions, section 3.3, and under block-on-ring conditions, section 3.2).

These phenomena are better explained by closer examination of the wear mechanisms. At lower magnification, abrasive grooves (as described e.g., in Ref 26) are seen both on the WC-12Co coatings (Fig. 9a, d) and on WC-10Co4Cr (Fig. 10a, d), but they are more marked in the latter case, consistent with their higher COW values (Fig. 3a). Magnified views indicate that wear damage mainly affects the matrix phase; indeed, the latter undergoes thermal softening [check for instance, the decrease in hardness of a typical Co-based alloy such as Stellite-6 from ≈ 360 HB at room temperature to HB at 540 °C (Ref 29)]. WC, by contrast, maintains nearly unaltered hardness up to ≈ 500 °C (Ref 30). As a larger fraction of the polished surface of the WC-12Co coatings is occupied by carbide grains, these samples suffer less damage (Fig. 9b, c, r, f) than the WC-10Co4Cr ones (Fig. 10b, c, e, f). The surface morphology, particularly with coarse carbides (Fig. 9d-f), suggests that wear, after initial removal of the matrix, proceeds by polishing of WC grains that are probably covered by a thin surface oxide layer, according to the same mechanism described for bulk (sintered) WC-Co cermet tools in (Ref 27). The friction coefficient, though higher than that measured at room temperature,

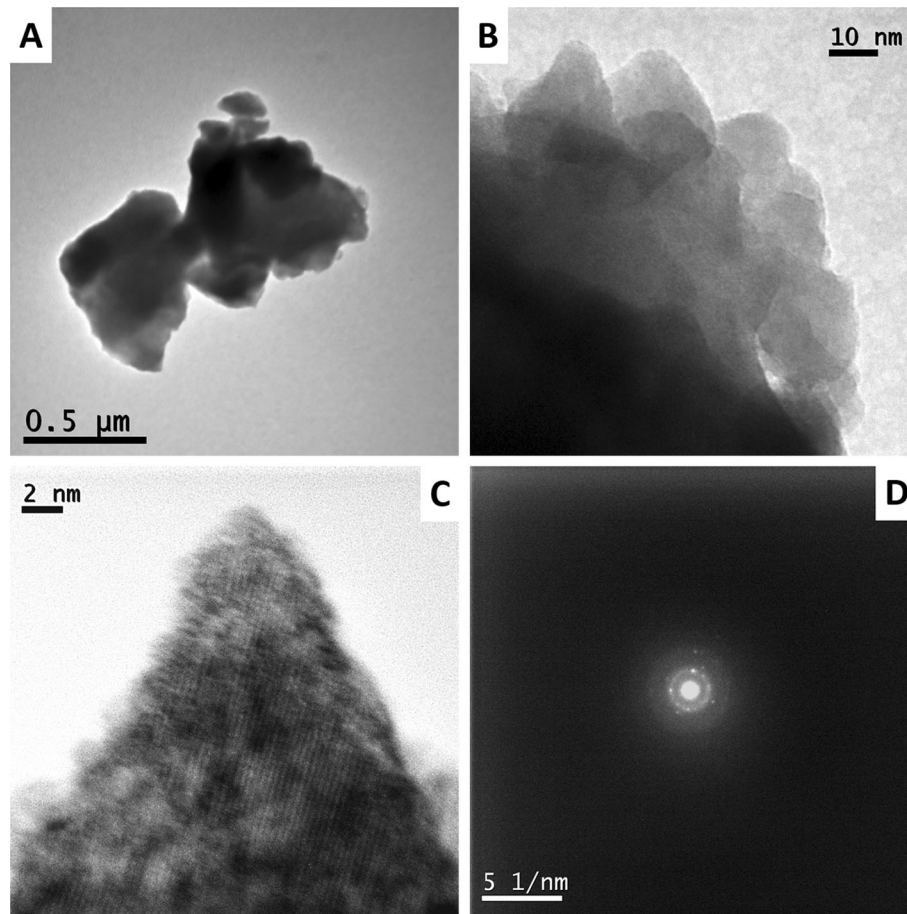


Fig. 7 TEM analysis of the loose wear debris collected after ball-on-disk sliding wear testing of sample P1K6 at room temperature: overview (a), detail (b), high-resolution view of a crystalline region (c), and selected-area diffraction (SAED) pattern (d) of the region seen in panel B

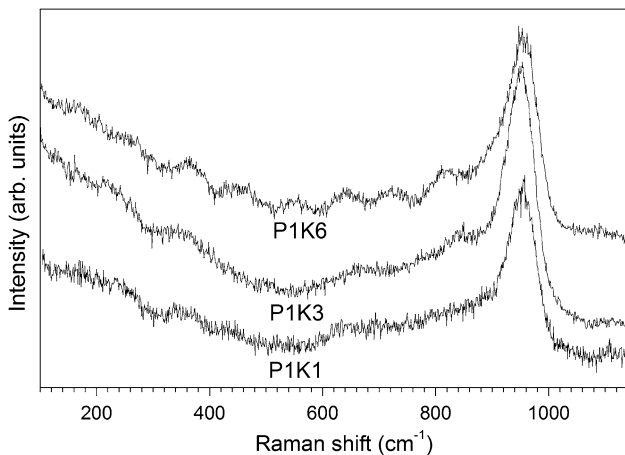


Fig. 8 Raman spectra acquired on the loose wear debris collected after ball-on-disk sliding wear testing of various samples at room temperature

remains ≤ 0.8 (Fig. 3b), and the surface of the Al_2O_3 counterpart remains clean and free of adherent transfer layers (Fig. 11a). In the WC-10Co4Cr coatings, by con-

trast, degradation and removal of the larger fraction of exposed matrix are clearly apparent from Fig. 10b, c, e, f. Friction coefficients accordingly rise to ≈ 0.95 -1.0 (Fig. 3b), indicating that, under these conditions, seizure between the WC-10Co4Cr coatings and their counterbody occurs. This also leads to the formation of (oxidized) wear debris, part of which is smeared onto the surface of the coating (resulting in the darker clusters seen in Fig. 10b, c, e, f) and of the counterpart (Fig. 11b). The formation of irregular, glazed debris layers on the mating bodies is typical of the tribo-oxidative wear of a metallic surface with high hardness sliding against a ceramic counterpart (Ref 28). This means the WC-CoCr samples exhibit “metal-like” wear behavior, consistent with the previous consideration on their higher initial matrix fraction. According to (Ref 28), friction can be high in spite of these irregular, oxidized layers, which matches well with the present observations.

In the case of fine CGS, however, a second wear mechanism also appears. Namely, microcracks are formed transversally across the wear scar, both in the case of WC-12Co samples (Fig. 9b, c: see arrows) and in WC-10Co4Cr ones (Fig. 10b, c: see arrows), and near-surface spallation

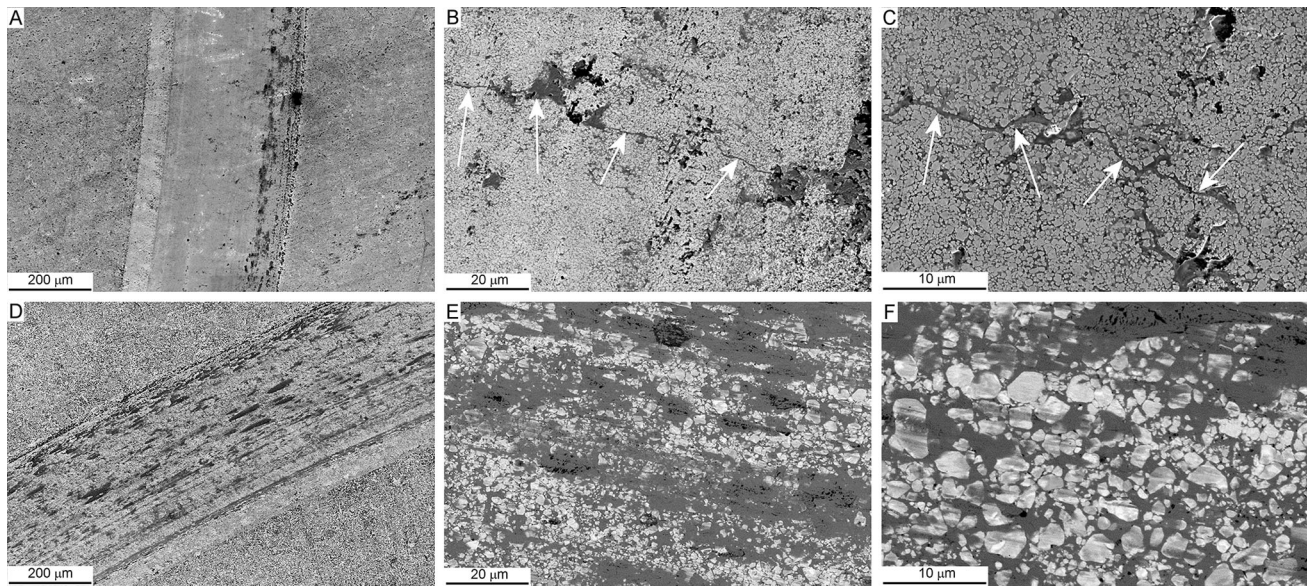
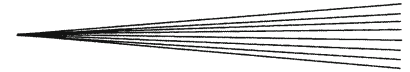


Fig. 9 SEM micrographs of the worn surfaces of samples P1K1 (a-c) and P1K3 (d-f) after ball-on-disk testing at 400 °C. The arrows in panels B,C indicate transverse microcracks across the wear track

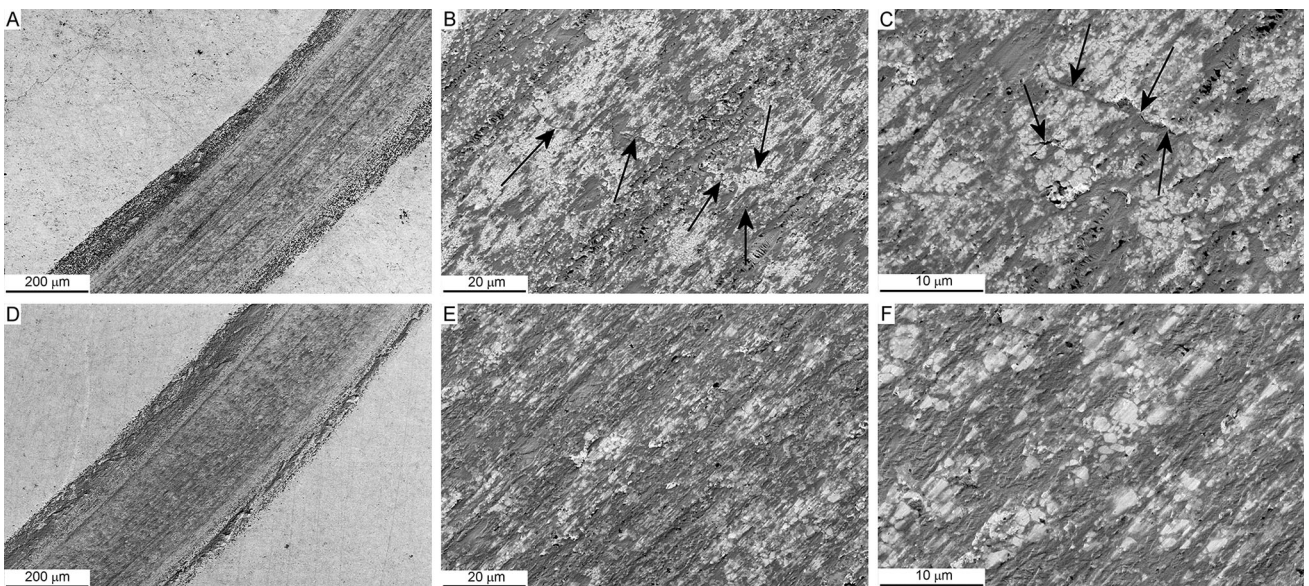


Fig. 10 SEM micrographs of the worn surfaces of samples P1K4 (a-c) and P1K6 (d-f) after ball-on-disk testing at 400 °C. The arrows in panels B,C indicate transverse microcracks across the wear track

of material consequently occurs. This mechanism clearly worsens the overall wear damage of the coating. For each coating material, coarse CGS samples produce slightly lower friction than fine or medium CGS ones (Fig. 3b) at 400 °C, which could explain the lower tendency of coarse CGS materials to develop such microcracks at high temperature. This is to be ascribed to the larger WC grains bearing a more significant portion of the contact load, as previously observed for room temperature tests in section 3.3 as well. It is also possible that, in fine-grained

samples, different micro-scale stress distributions can favor matrix failure and crack propagation. Similar micro-cracking was accordingly reported in previous papers for WC-10Co4Cr coatings having analogously fine CGS (Ref 6). In order to verify if the fine-grained samples have greater intrinsic brittleness than coarse-grained ones, scratch tests were performed on the WC-12Co samples with fine and coarse CGS (samples P1K1 and P1K3, respectively—see Table 1). Although these tests were run at room temperature (not at 400 °C), the results (Fig. 12)

clearly show that the coarse-grained samples have better resistance against transverse microcracking. Accordingly, the critical load for the onset of transverse microcracks (designated as L_{C1} in accordance with the nomenclature given in the ISO 20522 standard) in the two samples is $L_{C1} = (11 \pm 2)$ N for the fine-grained P1K1 sample and $L_{C1} = (22 \pm 3)$ N for the coarse-grained P1K3 sample. The behavior of coarse-grained coatings is therefore close to (even though not as good as) that of bulk WC-11%Co

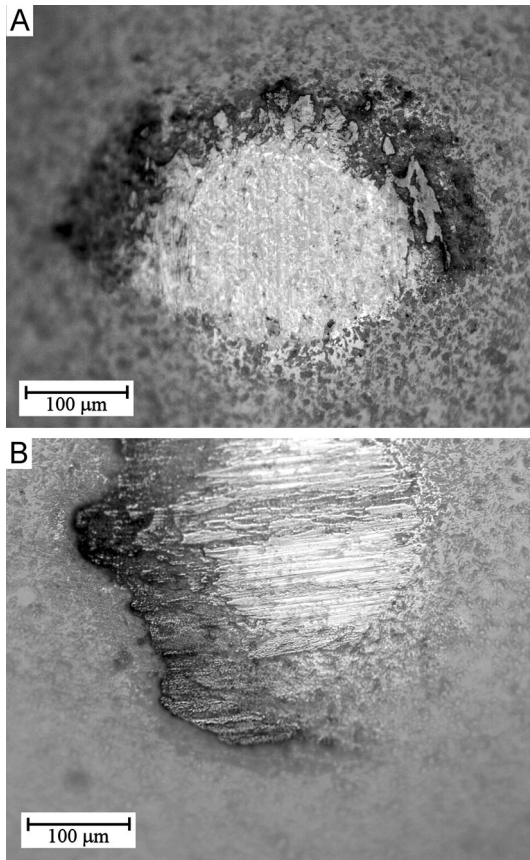


Fig. 11 Optical micrographs of the worn surfaces of the Al_2O_3 counterbody after ball-on-disk sliding wear testing against samples P1K3 (a) and P1K6 (b) at 400°C

cermets of similar CGS, which do not crack upon a single scratch pass of a $200\text{-}\mu\text{m}$ radius diamond tip at 30 N load (Ref 15).

Greater brittleness is also the most likely cause of the large wear damage of the HVOF-sprayed WC-10Co4Cr coating (Fig. 3a), whose COW is $>1 \times 10^{-6} \text{ mm}^3/(\text{Nm})$.

3.5 Cyclic Corrosion Tests

After 96 h of exposure in NSS environment, all WC-Co coatings corroded, whereas all WC-CoCr coatings surpassed the test, which highlights the passivation effect of chromium in the matrix. HVOF coatings outperform HVOF ones, and corrosion performance increases with coarsening the CGS above 192 h. After 40 h of exposure in AASS environment, HVOF coatings and the finest CGS HVOF coatings fail and corrode, for both feedstock powders. However, coarsening the CGS improves the AASS corrosion resistance up to 80 h for WC-Co HVOF coatings, and above 120 h for WC-CoCr HVOF ones. The accelerated corrosion test (Corrodokote) also confirms the better performance of the Cr-containing composition and the trend of improving corrosion resistance with coarser carbides (Fig. 13). The finer the carbides, the higher their

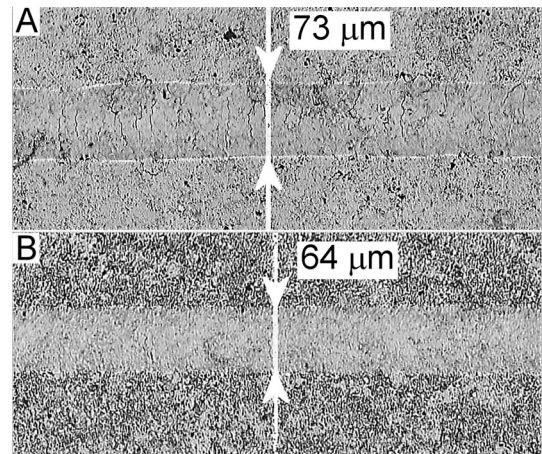


Fig. 12 Optical micrographs of the scratch tracks on the surfaces of samples P1K1 (a) and P1K3 (b): detail of the area corresponding to an applied normal load of 22 N

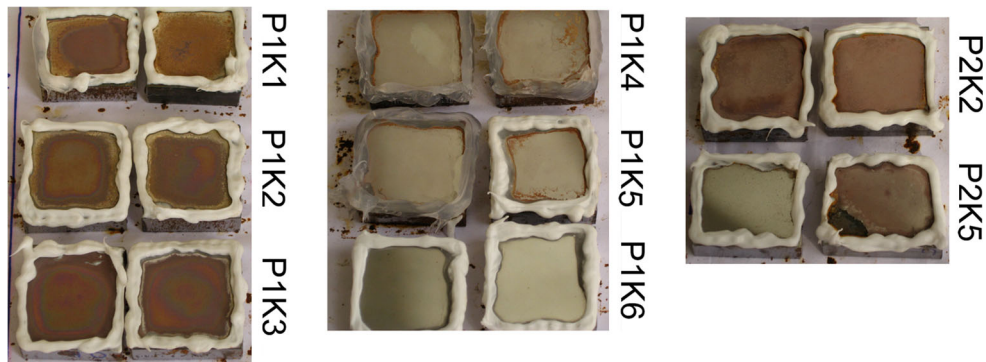


Fig. 13 Photographs of all samples after the 5th Corrodokote test cycle

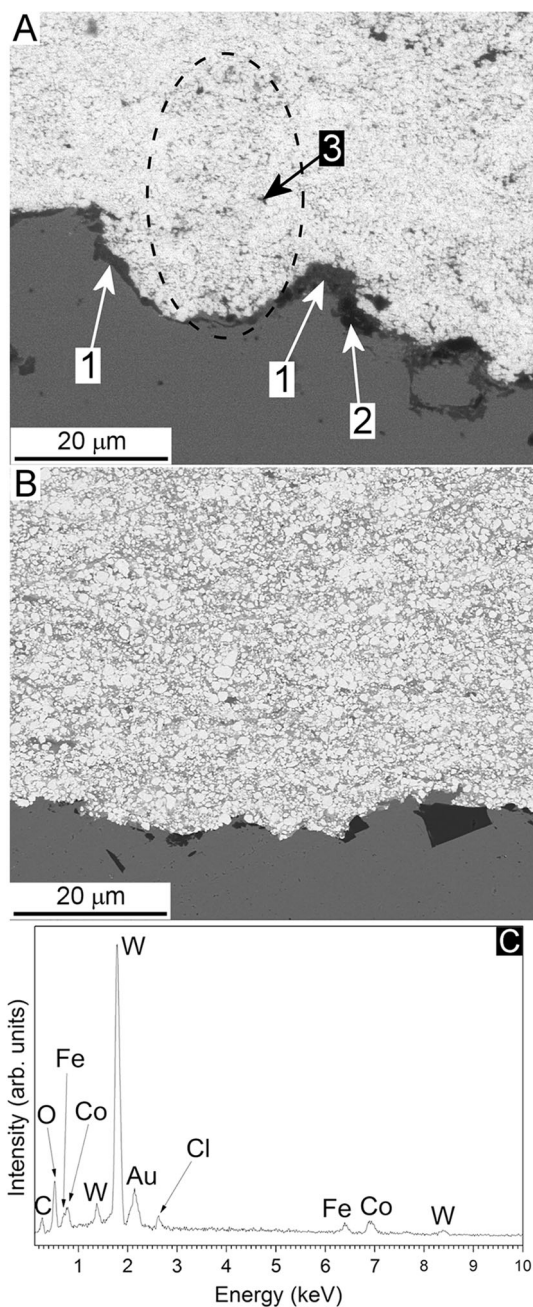


Fig. 14 SEM micrographs of the cross sections of samples P1K1 (a) and P1K6 (b) after 5 CorrodKote test cycles, and EDX spectrum (c) corresponding to the area labeled as “3” in panel A

specific surface, which increases the risk of interfacial galvanic coupling between the more noble carbides and less noble matrix phases. The corrosive solution generally propagates through the micro-pores network, selectively attacking the less noble matrix materials and opening up interconnected paths, through which it can reach the coating/substrate interface. One such interconnected path is marked by the circle in Fig. 14a. Due to the ingress of the corrosion products, a significant amount of corrosion products was developed at the coating/substrate interface (Fig. 14a, label 1); they are distinguishable from

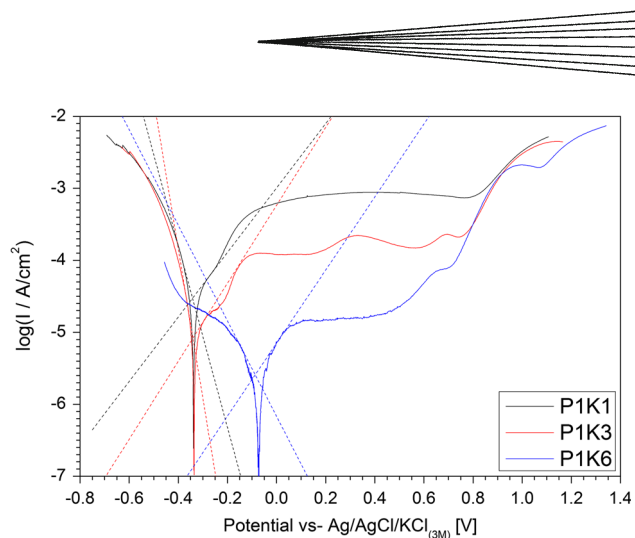


Fig. 15 Electrochemical polarization curves for some selected coating samples, with Tafel fitting

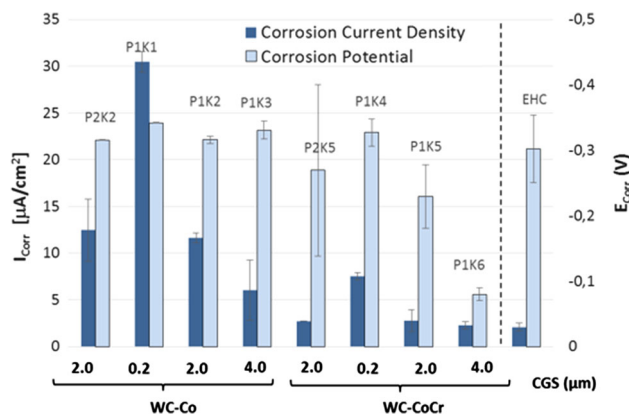


Fig. 16 Corrosion potential and current density results

the embedded alumina grits (Fig. 14a, label 2) because of their slightly different backscatter electron contrast. The corrosion products, having higher specific volume, infiltrate the interconnected pores (Fig. 14a, label 3—see the corresponding EDX spectrum in Fig. 14c) traveling toward the coating surface, where they emerge as seen in the photographs of Fig. 13. Some of the corrosion products by contrast, accumulate at the coating/substrate interface, where they might generate high pressure leading to coating delamination, as observed for the HVOF porous coating (P2K5: Fig. 13). By contrast, no opening of interconnected paths and no coating/substrate interface corrosion are observed in the coarse carbide coatings (Fig. 14b).

3.6 Polarization Test

Corrosion current density (I_{Corr}) and Potential (E_{Corr}) values were evaluated by the Tafel method as shown in Fig. 15. HVOF-sprayed coatings exhibited identical I_{Corr} than HVAF-sprayed ones for identical medium CGS size (Fig. 16). The corrosion performance was improved with coarsening the CGS for both feedstock powders. Reduction of both I_{Corr} and E_{Corr} for WC-CoCr materials, compared

to WC-Co coatings, confirmed the passivation effect of Cr matrix, which is clearly seen through the polarization curves in Fig. 15. The Cr-containing sample obtained from the coarse CGS feedstock indeed attains a pseudo-passive state with current density values of $\approx 1.5 \times 10^{-5}$ A/cm² until an apparent breakdown of passivity occurs at a potential of about +500 mV versus Ag/AgCl/KCl_(3M). As thoroughly described in the literature (Ref 31, 32), pseudo-passivation is due to a partially protective oxide layer on the matrix phase, whereas the apparent breakdown is due to the corrosion rate of WC becoming faster than that of the matrix. Sample P1K3 exhibits comparatively larger pseudo-passive current density of $\approx 1.5 \times 10^{-4}$ A/cm², which is closer to the values typical of sintered pure WC-Co cermets (Ref 31, 32) (Fig. 15). With fine carbides, the current density values further increase due to the ingress of the corrosive medium into the open pores, down to the substrate, as shown previously. Sample P1K6 exhibited similar I_{Corr} but a significantly nobler E_{Corr} than the EHC reference sample (Fig. 16).

4. Conclusion

For both powder feedstock materials, coarsening the CGS leads to increasing coating density and improving the carbide-matrix interfaces by decreasing both carbides and contiguity densities (D_{CGS} and D_{CC}), while increasing the MFP density (DM_{FP}), highlighted by the respective increase of the binder volume fraction. The main consequences are as follows: (1) the reduction of the permeability to corrosive solutions, with a general improvement of coating corrosion resistance, more pronounced for the Cr-containing metallic binder presenting passivating effect; and (2) the improvement of sliding wear resistance of coatings presenting micro-scale plastic deformation and cracking at the intra-lamellar level, a phenomenon more pronounced for Co matrix than for CoCr material. However, the CGS ratio to the binder size relatively to the initial powder grain strength of the feedstock material needs to be further investigated, in order to fully understand the tribological behaviors of such HVAF-sprayed coatings, under different sliding wear conditions.

Acknowledgments

The authors gratefully acknowledge SP Institute (Borås, Sweden) for NSS and AASS corrosion investigations, and Carolina Pettersson at SWEREA IVF (Mölnådal, Sweden) for her contribution to SEM analysis at high magnification.

References

1. M. Bielewski, Replacing Cadmium and Chromium, Research and Technology Organization and NATO, RTO-AG-AVT-140, 2011, Chp.23, pp. 1-22
2. L.-M. Berger, P. Vuoristo, T. Mäntylä, W. Kunert, W. Lengauer, and P. Eittmayer, *Practical Solutions to Engineering Problems*, C.C. Berndt, Ed., ASM International, Materials Park, OH, 1996, p 97-106
3. G. Bolelli, R. Giovanardi, L. Lusvarghi, and T. Manfredini, Corrosion Resistance of HVOF-Sprayed Coatings for Hard Chrome Replacement, *Corros. Sci.*, 2006, **48**, p 3375-3397
4. A. Wank, B. Wielage, H. Pokhmurska, E. Friesen, and G. Reisel, Comparison of Hardmetal and Hard Chromium Coatings Under Different Tribological Conditions, *Surf. Coat. Technol.*, 2006, **201**, p 1975-1980
5. G. Bolelli, L.-M. Berger, M. Bonetti, and L. Lusvarghi, Comparative Study of the Dry Sliding Wear Behaviour of HVOF-Sprayed WC-(W, Cr)2C-Ni and WC-CoCr Hardmetal Coatings, *Wear*, 2014, **309**, p 96-111
6. G. Bolelli, L.-M. Berger, T. Börner, H. Koivuluoto, L. Lusvarghi, C. Lyphout, N. Markocsan, V. Matikainen, P. Nylén, P. Sassatelli, R. Trache, and P. Vuoristo, Tribology of HVOF- and HVAF-Sprayed WC-CoCr Hardmetal Coatings: A Comparative Assessment, *Surf. Coat. Technol.*, 2015, **265**, p 125-144
7. Q. Wang, S. Zhang, Y. Cheng, J. Xiang, X. Zhao, and G. Yang, Wear and Corrosion Performances of WC-10Co4Cr Coatings Deposited by Different HVOF and HVAF Spraying Processes, *Surf. Coat. Technol.*, 2013, **218**, p 127-136
8. M. Barletta, G. Bolelli, B. Bonferroni, and L. Lusvarghi, Wear and Corrosion Behaviour of HVOF-Sprayed WC-CoCr Coatings on Al Alloys, *J. Therm. Spray Technol.*, 2010, **19**(1-2), p 358-367
9. ASTM G99-05, Standard Test Method for Wear Testing with a Pin-on-Disk Apparatus, ASTM International, West Conshohocken, PA, 2010, www.astm.org
10. ASTM G77-, Standard Test Method for Wear Testing with a Ball-on-Disk Apparatus, ASTM International
11. S. Luyckx and A. Love, The Dependence of the Contiguity of WC on Co Content and Its Independence from WC Grain Size in WC-Co Alloys, *Int. J. Refract. Metals Hard Mat.*, 2005, **V24**, p 75-79
12. C. Lyphout, J. Kitamura, K. Sato, J. Yamada, and S. Dizdar, Tungsten Carbide Deposition Processes for Hard Chrome Alternative: Preliminary Study of HVAF vs. HVOF Thermal Spray Processes, *Proceedings ITSC 2013*, Busan, South Korea, 2013
13. C. Lyphout, S. Björklund, M. Karlsson, M. Runte, G. Reisel, and P. Boccaccio, Screening Design of Supersonic Air Fuel Processing for hard Metal Coatings, *J. Therm. Spray Technol.*, 2014, **23**(8), p 1323-1332
14. C. Lyphout and K. Sato, Screening Design of Hard Metal Feedstock Powders for Supersonic Air Fuel Processing, *Surf. Coat. Technol.*, 2014, **258**(2014), p 447-457
15. J.C.P. Zuñega, M.G. Gee, R.J.K. Wood, and J. Walker, Scratch Testing of WC/Co Hardmetals, *Tribol. Int.*, 2012, **54**, p 77-86
16. G. Bolelli, A. Candeli, H. Koivuluoto, L. Lusvarghi, T. Manfredini, and P. Vuoristo, Microstructure-Based Thermo-Mechanical Modelling of Thermal Spray Coatings, *J. Therm. Spray Technol.*, 2015, **24**(15), p 20-34
17. W.A. Glaeser, Wear Debris Classification, *Modern Tribology Handbook—Volume One—Macrotribology*, B. Bhushan, F.E. Kennedy, and A.Z. Szeri, Ed., CRC Press, Boca Raton, Florida (USA), 2001, p 301-315
18. J.V. Gabrusenoks, P.D. Cizmach, A.R. Lulis, J.J. Kepleris, and G.M. Ramans, Electrochromic Colour Centres in Amorphous Tungsten Trioxide Thin Films, *Solid State Ionics*, 1984, **14**, p 25-30
19. M.F. Daniel, B. Desbat, J.C. Lassegues, B. Gerand, and M. Figlarz, Infrared and Raman Study of WO₃ Tungsten Trioxides and WO₃·xH₂O Tungsten Trioxide Hydrates, *J. Solid State Chem.*, 1987, **67**, p 235-247
20. S. Usmani, S. Sampath, D.L. Houck, and D. Lee, Effect of Carbide Grain Size on the Sliding and Abrasive Wear Behavior of Thermally Sprayed WC-Co Coatings, *Tribol. Trans.*, 1997, **40**(3), p 470-478
21. T. Sudprasert, P.H. Shipway, and D.G. McCartney, Sliding Wear Behaviour of HVOF Sprayed WC-Co Coatings Deposited With Both Gas-Fuelled and Liquid-Fuelled Systems, *Wear*, 2003, **255**, p 943-949



22. Q. Yang, T. Senda, and A. Ohmori, Effect of Carbide Grain Size on Microstructure and Sliding Wear Behavior of HVOF Sprayed WC-12% Co Coatings, *Wear*, 2003, **254**(1-2), p 23-34
23. Q. Yang, T. Senda, and A. Hirose, Sliding Wear Behavior of WC-12% Co Coatings at Elevated Temperatures, *Surf. Coat. Technol.*, 2006, **200**(14-15), p 4208-4212
24. C. Verdon, A. Karimi, and J.-L. Martin, A Study of High Velocity Oxy-Fuel Thermally Sprayed Tungsten Carbide Based Coatings. Part 1: Microstructures, *Mater. Sci. Eng. A*, 1998, **246**(1-2), p 11-24
25. L.-M. Berger, R. Puschmann, J. Spatzier, and S. Matthews, Potential of HVOF Spray Process, *Therm. Spray Bull.*, 2013, **6**(1), p 16-20
26. G.W. Stachowiak and A.W. Batchelor, *Engineering Tribology*, 2nd ed., Butterworth-Heinemann, Woburn, MA, 2001, p 483-531
27. I. Konyashin, Cemented Carbides for Mining, Construction and Wear Parts, *Comprehensive Hard Materials—Volume I: Hardmetals*, V.K. Sarin, D. Mari, L. Llanes, and C.E. Nebel, Ed., Elsevier, Amsterdam, The Netherlands, 2014, p 425-451
28. G.W. Stachowiak and A.W. Batchelor, *Engineering Tribology*, 2nd ed., Butterworth-Heinemann, Woburn, MA, USA, 2001, p 560-569
29. J.R. Davis, Ed., *ASM Specialty Handbook: Nickel, Cobalt, and Their Alloys*, ASM International, Materials Park, OH, USA, 2000, p 382-383
30. A.S. Kurlov and A.I. Gusev, Tungsten Carbides—Structure, Properties and Application in Hardmetals, *Springer Series in Materials Science*, Vol 184, R. Hull, C. Jagadish, R.M. Osgood, J. Parisi, and Z.M. Wang, Ed., Springer, Cham, 2013, p 34-36
31. A.M. Human and H.E. Exner, The Relationship Between Electrochemical Behaviour and In-service Corrosion of WC Based Cemented Carbides, *Int. J. Refract. Met. Hard Mater.*, 1997, **15**, p 65-71
32. A.M. Human and H.E. Exner, Electrochemical Behaviour of Tungsten-Carbide Hardmetals, *Mater. Sci. Eng. A*, 1996, **209**, p 180-191